

# DNS of laminar-turbulent boundary layer transition induced by solid obstacles

P. Orlandi S. Pirozzoli , & M. Bernardini

*Dipartimento di Ingegneria Meccanica e Aerospaziale  
Università La Sapienza, Via Eudossiana 16, I-00184, Roma*

---

## Abstract

Results of numerical simulations obtained by a staggered finite difference scheme together with an efficient immersed boundary method are presented to understand the effects of the shape of three-dimensional obstacles on the transition of a boundary layer from a laminar to a turbulent regime. Fully resolved Direct Numerical Simulations (DNS), highlight that the closer to the obstacle the symmetry is disrupted the smaller is the transitional Reynolds number. It has been also found that the transition can not be related to the critical  $R_k = U_k k / \nu$  used in the past. The simulations highlight the differences between wake and inflectional instabilities, proving that two-dimensional tripping devices are more efficient in promoting the transition. Simulations at high Reynolds number demonstrate that the reproduction of a real experiment with a solid obstacle at the inlet is an efficient tool to generate numerical data bases for understanding the physics of boundary layers. The quality of the numerical method to fully resolve the small scales, that is one ingredient for a DNS was shown by a comparison of the exponential range of the velocity spectra, in Kolmogorov units, with those for isotropic turbulence. The good comparison reinforces the idea of local isotropy at the

smallest scales.

*Keywords:*

Transition, Roughness, Direct Numerical Simulation, Immersed boundary

---

## 1. Introduction

The laminar-turbulent transition of boundary layers is of large importance in several practical applications and in particular for the aeronautical industry. Naturally it occurs when external disturbances affect the near wall region, generating turbulent spots (Emmons [6]) occurring randomly and growing uniformly independently of one another as they are swept downstream by the flow. More efficiently, the transition can be promoted by inserting solid obstacles on a smooth wall at a certain distance from the leading edge. Therefore the shape of the elements may play an effect on the location at which the flow becomes turbulent. The tripping device can be obtained by a series of obstacles widely separated (three-dimensional) or by a wire in the whole span (two-dimensional). Different scenarios can be achieved, for the former configuration the transition can be classified as a wake instability, which is associated to the generation of vorticity layers at the obstacle walls which evolve in the streamwise direction. For disturbances in the whole span of the plate an inflectional point in the velocity profile inside the recirculating region behind the obstacle appear. Therefore the small disturbances grow rapidly and a turbulent flow is generated in the whole boundary layer. Klebanoff *et al.* [17] wrote an exhaustive paper on the transition of boundary layers induced by solid elements, claiming that two-dimensional obstacles are more efficient to excite three-dimensional disturbances than the oscillating

ribbon previously used (Klebanoff *et al.* [16]). The Klebanoff study had such impact that this type of laminar-turbulent transition was defined as Klebanoff transition.

Klebanoff *et al.* [17] used hemispherical obstacles with an aspect ratio equal to 1 and height  $k$  smaller than the boundary layer thickness  $\delta$ . They compared the values of the transition Reynolds number ( $R_k = U_k k / \nu$ , where  $U_k$  is the velocity of the undisturbed flow at the top of the element) with those obtained in other experimental setup. Large differences were found, for instance their value equal to 325 was different than those in Tani *et al.* [32], varying between 600 and 1000. Dryden [5] emphasized that, once the transition occurred, a further increase of the Reynolds number had the effect of moving the location of the transition upstream. The reasons of the differences in the critical  $R_k$  depend on the nature of the laminar-turbulent transition. For instance for isolated obstacles it occurs at a certain distance from the obstacle rather smoothly, and each scholar used different criteria to establish when the turbulent flow is assessed. In the discussion of the results Klebanoff *et al.* [17] claimed that the shape of the obstacle plays a role and that the data in literature were limited. For us this assertion is still true and hence it has been decided to give a contribution to understand the effects of the shape of the obstacles by numerical simulations.

The Klebanoff's transition was reconsidered experimentally and numerically by Bake *et al.* [2]. However, the DNS was performed by taking the disturbances from the experiments and it was observed that the vortical structures responsible for the transition consisted in series of  $\Lambda$ -shaped vortices. Ergin & White [9], analysing the experimental results, related the

transitional mechanism to the shape of the optimal disturbances producing the largest growth over a specified distance or time. They claimed that these disturbances are similar to those produced by three-dimensional obstacles. Flow visualizations as that by Acarlar & Smith [1] have shown that three-dimensional obstacles in a laminar boundary layer generate horseshoe vortices wrapping around the upstream side of the obstacle with the two legs downstream. Flow visualizations are qualitative and quantitative measurements are difficult, in particular to have insights on the effect of the shape of the obstacle. Acarlar & Smith [1] for clear flow visualizations used obstacles with  $k/\delta = 1$  different from those typical of the tripping devices and different from those used by Klebanoff *et al.* [17]. Therefore, they got different profiles for the streamwise velocity fluctuations. In discussing the reason of the differences and on the possibility to find a scaling of the transition, Klebanoff *et al.* [17] were asking for further investigations. Ergin & White [9] designed their experiments to understand the flow behavior in the Kendall's near and far wake (Kendall [15]). In the near wake region the energy of the disturbance decreases; in the far wake, depending on the Reynolds number, the growth is similar to the optimal growth predicted by the theory. Ergin & White [9] used an array of cylindrical elements separated by a distance such that the elements can be considered isolated. They did not change the shape of the obstacles and they still used the critical  $R_k$  as a parameter to establish when the flow becomes turbulent.

Our opinion is that  $R_k$  can not mark the transition from laminar to turbulent flow. The  $R_k$  should be replaced by a quantity related to the velocity disturbance generated by the solid obstacle. In wall bounded turbulent flows

the normal to the wall velocity fluctuations ( $u'_2$ ) are those producing the turbulent Reynolds stress  $\langle u'_1 u'_2 \rangle$  characteristic of the turbulent regime (the index  $i = 1$  indicates streamwise,  $i = 2$  normal and  $i = 3$  spanwise directions, angular brackets  $\langle \rangle$  averages in the homogeneous directions and in time). These fluctuations produce also  $\langle u'^2_2 \rangle$ , the only normal stress entering in the mean momentum equations, for channel and pipes. For boundary layers other stresses appear, but the relative terms are one order of magnitude smaller. In wall bounded flows the importance of  $\langle u'^2_2 \rangle$  was not emphasized in the early experiments, designed to understand the physics of the near wall turbulence, for the difficulties to measure  $u_2$ , close to a wall, by hot wires. In numerical simulations all the quantities are available and in addition the boundary conditions at the surface can be arbitrarily varied. For instance, in turbulent channels, Orlandi *et al.* [23] demonstrated that, the normal velocity distribution on the plane of the crests is the driving mechanism for the modifications of the near wall structures. The preliminary results suggested that, a new parametrisation for rough flows could be obtained by  $\tilde{u}'_2|_k$ , with  $\tilde{u}'_i = \langle u'^2_i \rangle^{1/2}$  ( $|_k$  indicates values at the plane of the crests). A continuous transition between smooth ( $\tilde{u}'_2|_k = 0$ ) and rough walls ( $\tilde{u}'_2|_k \neq 0$ ) was observed. The importance of this quantity has been further emphasized by Orlandi [20] performing DNS of transitional channels with different type of solid disturbances in one wall of the channel. It was observed that the flow in the channel becomes turbulent when  $\tilde{u}'_2|_k^+ > 0.2$  (the superscript  $+$  indicates wall units). However when this threshold is achieved, the smallest value for turbulent flows is  $\tilde{u}'_2|_k^+ = 0.6$ . By increasing the Reynolds number there is a growth of this stress tending to a value approximately equal to 1, which is

also the value of the maximum  $\tilde{u}_2'^+$  in smooth pipes or channels.

Bake *et al.* [2] introduced normal velocity disturbances at the wall derived by laboratory experiments designed ad hoc. From the previous arguments a similarity between a solid obstacle and a distribution of  $u_2$  at the wall, for instance a round jet, does exist. Therefore for rough boundary layers  $\tilde{u}_2'$  could be a quantity whose value when overcomes a threshold value detect the laminar-turbulence transition. Regarding the transition this quantity can not replace the  $R_k$  criterium because it can not be apriori estimated, but qualitatively it can help to design the optimal shape of the obstacle producing the highest value at the top, this is out of the scope of the present paper. The strategy to change the shape of the obstacle helps to demonstrate that  $R_k$  can not mark the transition. In fact for certain geometries the transition may occur and for others no, even if  $R_k$  does not largely varies. A further interest is to investigate whether the numerical simulation of a laminar inlet flow past a solid obstacle can be an affordable procedure to get turbulent boundary layers at high Reynolds number. To reach these goals it is necessary to understand which tripping device gives the fastest growth and to have a quantitative measure of the transitional distance necessary to get a fully turbulent regime. The first DNS of boundary layers by Spalart [31] used a pseudo-spectral numerical method together with a fringe method to recycle the output flow to the inlet. More sophisticated recycling methods were developed as reported by Pirozzoli & Bernardini [25] in DNS of compressible turbulent boundary layers. Simens *et al.* [30] asserted that with a distance of 300 momentum initial thickness the influence of the artificial inlet conditions are eliminated. Lee *et al.* [18] used similar inlet conditions in presence of

rough walls. In these conditions the disturbances, continuously emanating from the interior of the rough surfaces, reduce the distance to achieve a fully turbulent rough boundary layer. Wu & Moin [33] simulated the whole transitional flow by adding to the potential flow patches of isotropic turbulence. This disturbance can be considered an attempt to reproduce the conditions in wind tunnels similar to those by Emmons [6], where turbulence grows as random organised turbulent spots. More recently Schlatter *et al.* [27] used a low-amplitude trip force acting in the wall-normal direction. In this way they had a rapid laminar-turbulent transition close to the inlet. The authors did not furnish the velocity distributions so it is difficult to connect the disturbance to a real tripping device.

With the exception of the DNS of rough boundary layers (Lee *et al.* [18]) the numerical methods in the mentioned simulations did not allow to reproduce the flow interaction with solid obstacles. The numerical method used in this paper (Orlandi & Leonardi [21]) is based on a second order finite difference method and on an immersed boundary technique (IBM) to reproduce bodies of any shape. The method was tested in previous papers and in particular it was shown by Orlandi *et al.* [22] that the pressure distribution on the rod-shaped elements was in a very good agreement with those measured by Furuya *et al.* [11]. In addition a combined experimental-numerical study (Burattini *et al.* [4]) was performed to validate the DNS, with square bars with  $w/k = 3$  ( $w$  is the spacing between two elements). The basic numerical method requires small modifications to deal with boundary layers. Radiative outlet boundary conditions allow to the vortical structures to exit smoothly from the computational domain. The modifications in time and space of

the three components of the vorticity fields, near the solid element, allows to understand why at the same Reynolds number for some geometries are amplified and for others are not. A comparison between coarse and refined simulations (not presented) suggests that the inaccurate representation of the surface acts as disturbances reducing the critical Reynolds number, therefore small imperfections in a solid obstacle while do not change  $R_k$  would enhance the transition, this is a further reason of the inadequacy of  $R_k$  to mark the transition.

## 2. Numerical method

The basic numerical method consists of a second order finite difference scheme with staggered velocities, which in the inviscid limit conserves total energy. The method for the channel is described in Orlandi [19] where the global conservation properties in presence of non-uniform grids in the normal directions are presented. The boundary layers simulations require inlet, outlet and initial conditions. The radiative conditions at the outlet (Pauley *et al.* [24]) allow the flow vortical structures to exit from the computational domain without producing disturbances, which propagating backwards can affect the flow. In these circumstances, a cos FFT is necessary to have a direct flow solver for the elliptic equations necessary to have a solenoidal velocity field. At the inlet a Blasius velocity profile is imposed by fixing the Reynolds number and the distance from the leading edge. The theory of laminar boundary layers allows to derive at  $t = 0$  the streamwise and normal velocity profiles in the entire computational domain. This two-dimensional flow is replicated in the whole spanwise direction, and small random distur-



bances are added at the inlet to trigger the spanwise disturbances, which, interacting with the large scale created by the obstacles at the supercritical Reynolds number, produce a turbulent flow.

The Navier-Stokes and the continuity equation in dimensionless form, are

$$\frac{\partial u_i}{\partial t} + \frac{\partial u_i u_j}{\partial x_j} = -\frac{\partial p}{\partial x_i} + \frac{1}{Re} \frac{\partial^2 u_i}{\partial x_j^2} ; \quad \frac{\partial u_i}{\partial x_i} = 0 . \quad (1)$$

where  $p$  is the dimensionless pressure. The Reynolds number is defined as  $Re = U_e \delta / \nu$ , being  $U_e$  the constant free-stream velocity and  $\delta$  the boundary layer thickness at the inlet section (usually indicated as  $\delta_{99}$ ) .

The solid element is located at a distance  $x_0$  from the inlet, whose effect on the flow is reproduced by an immersed boundary technique. The efficiency of the method together with the MPI (Message Parallel Interface) instructions allow to use a sufficient number of grid points to describe the body surface. The IBM method differs from that developed by Fadlun *et al.* [10], where the velocities at the nearest points to the surface were evaluated by interpolations. Indeed Orlandi & Leonardi [21], after the evaluation of the right hand side of the discretized equations in the regular grid, correct the viscous terms, in the explicit and implicit step. For the flows here considered where the obstacles do not move, the metrics coefficients at the nearest points are calculated only once initially.

### 3. Results

#### 3.1. Low and medium Reynolds number

A first set of simulations were performed on a coarse grid with  $512 \times 128$  points in the streamwise and spanwise directions respectively. In the normal

direction a non-uniform grid was used with 50 grid points for  $0 < x_2 < 1$  and 50 for  $1 < x_2 < 10$ . The three-dimensional solid obstacles have aspect ratio equal to 1 and a dimensionless height  $k = 0.25$ . The computational box, for the coarse simulations, has  $L_1 = 25.6$  and  $L_3 = 3.2$ . With these parameters the solid elements are described by 5 points in  $x_1$  and  $x_3$  and 25 points in  $x_2$ . Such coarse grid was chosen on the purpose to investigate the dependence of the results on the shape of the element. Three-dimensional solid disturbances with cylindrical, cubic and wedge shape were used. The experimental results described by Klebanoff *et al.* [17] showed that two-dimensional obstacles behave differently than three-dimensional obstacles. Therefore an additional set of simulations with a square rod, located at the same distance from the inlet ( $x_0 = 5$ ) were performed.

These simulations showed that for the cylinder the transition Reynolds number was higher than that for the cubic obstacle. The latter did not largely differ from that for the wedge. It was also observed that for square bars the critical Reynolds number was much smaller than that for the three-dimensional obstacles. From these results it was decided to look at the transition mechanism for the cubic obstacle by varying the  $Re$  number in a well resolved simulations with  $1024 \times 160 \times 192$  grid points in a domain with the same size above cited. The obstacles is, then, descibed by  $10 \times 15$  grid points in  $x_1$  and  $x_3$ . The occurrence of transition was detected by monitoring the time evolution of of  $\omega_3$  at  $x_2 = 0.0041$  and  $x_3 = 1.6$ .

As it was previously mentioned, an unsteady simulation evolves towards a stationary condition, that depending on the value of  $Re$ , remains laminar or becomes turbulent. In both cases the transient time necessary to the

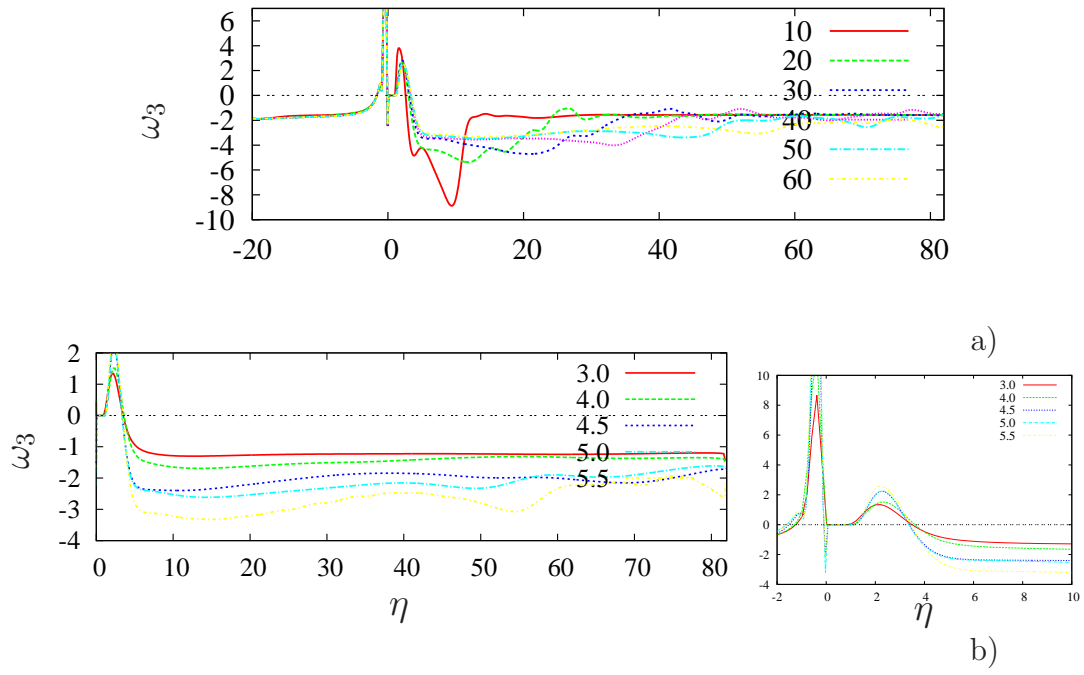


Figure 1: Streamwise profiles of  $\omega_3$  versus  $\eta = (x - x_0)/k$  at  $y/\delta = 0.0041$  at  $t = 10, 20, 30, 40, 50$  and  $60$  for a) the cube at  $Re = 5500$   $t$  is indicated in the figures, b) the cube at  $t = 60$  and different  $Re10^3$  as in the inset.

disturbance, produced by the obstacle, to reach the outlet boundary, depends on  $L_1$ . Figure 1a shows the trends at  $Re = 5500$ , where upstream of the obstacle is found a high positive peak, due to the formation, of the opposite sign vorticity characterising the head of the horseshoe vortex. Behind and close to the obstacle the other positive peak is due to the three-dimensional separation bubble, which does not depend on time, and weakly is affected by  $Re$ . When the flow reattaches the wall vorticity varies with  $Re$  and with time. The profiles at low  $Re$  show that the negative bump, while is convected downstream, decreases its amplitude for viscous effects, and the disturbance does not reach the outlet section. Figure 1a at  $Re = 5500$  shows that after the short transient, ending at  $10 < t < 20$ , the disturbance travels downstream without an appreciable reduction for viscous effects. Figure 1b with the profiles at different  $Re$  show at  $Re = 4000$  the behavior, similar to that at  $Re = 3000$ , suggesting a critical  $R_{cr}$  close to 4500, which leads to  $R_k = 400$  not too different from that observed in the experiments. The transition starts near the outlet section and this figure demonstrates that the simulations reproduce the Dryden [5] observations of the upstream movement of the transition location with the increase of  $Re$ . The zoom of the region near the obstacle (figure 1b) emphasizes that, only for  $Re > 4000$ , in front of the obstacle  $\omega_3$  is negative indicating the presence of an intense horseshoe vortex.

To have a better understanding of the influence of the shape of the vortical structures more shapes have been considered at  $Re = 5500$ . In figure 2 the contour plots of  $u_1$ , in a small region surrounding the body, allow to get an idea of the accurate reproduction of the flow near the body. In addition these

contours depict the shape of the obstacles considered: a) cylinder (*CY*), b) cube (*CU*), c) a wedge pointing upstream (*WU*), d) a wedge pointing downstream (*WD*), e) half cylinder with straight wall upstream (*SU*) and f) with the straight wall downstream (*SD*). The contours at a distance from the wall  $x_2 = 0.15$  highlight the shape of the separation bubble. The head of the horseshoe vortex does not reach this height then does not appear in figure 2. The square bar has been, also, considered (*SQ*), but for this two-dimensional obstacle the geometry is simple and contour plots of  $u_1$  are not given. To emphasize the shape of the separated region, the  $\Delta u_1$ , for the negative values, has been reduced ten times. In figure 2 the smooth contours, and, hence, the absence of numerical oscillations stress the accuracy of the immersed boundary technique to reproduce the effects of solid walls. The different amplitude of the perturbations, in the region close and downstream of the separation bubble is a first indication that for the *SU* and *SD* obstacles there is the transition. In addition it can be speculated that for *SD* the transition starts closer to the obstacles. Similar perturbations are observed for *WD*, having a smaller amplitude and being more symmetric the transition moves downstream. For the the other three geometries no any idea can be drawn by these images.

To have more quantitative results the spanwise averaged  $C_f = 2S_w/Re$  ( $S_w = \frac{\partial U}{\partial y}|_w$ ) has been evaluated by saving eleven fields from  $t = 60$  to  $t = 70$  separated by one time unit. It can be argued that a more interesting quantity should be the  $\omega_3|_w$  at  $x_3 = 1.6$  plotted in figure 1a with streamwise oscillations in the turbulent region. To have smooth profiles the simulations should evolve for a long time. To detect the difference in the growth between the

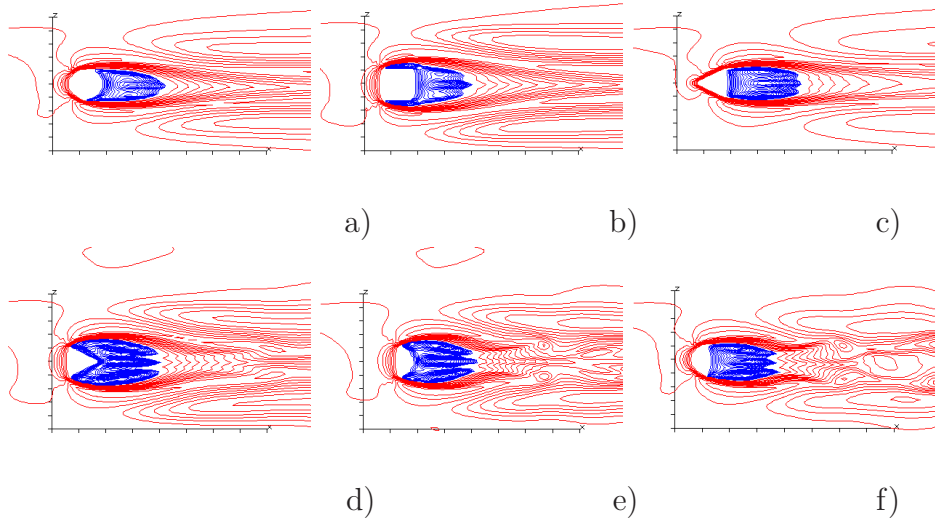


Figure 2: Streamwise velocity profiles at  $y/k = 0.6$  for the three-dimensional obstacles simulations described in a grid with 10 points in  $x_1$  15 in  $x_3$  and 40 in  $x_2$ . The height of the obstacle is  $k = 0.25$ ; red dashed positive, blue solid negative and  $\Delta u_1 = 0.025$  for the red and  $\Delta u_1 = 0.0025$  for the blue lines.

laminar and the turbulent regime by smoother curves a further averaging in  $x_3$  may help. For the cylinder in figure 3a there is no transition. For the cube the transition is not close to the obstacle. To understand the reasons of the transition the surface contours of  $\omega_3$  and  $\omega_2$  may help, as it is discussed later on. In figure 2b the flow is symmetric with respect to the centerline, which is an indicator of the absence of turbulence formation within a reasonable distance from the obstacle. A good level of symmetry is also obtained for the *WU* obstacle, where thin layers of high velocity gradients form (figure 2c). These being more unstable, produce the transition at a reasonable distance from the obstacles, as it results in figure 3a. The transition is close to the obstacle for the other three shapes and to stress the differences, in figure 3b the enlargement of the region with the  $C_f$  growth confirms the discussion derived from figure 2. The different growth is appreciated only at  $Re$  close to  $R_{cr}$ . At high Reynolds number these differences disappear, and, later on, is shown that for the cube, the fully turbulent  $C_f$  tends to that of a two-dimensional square bar. The interesting result of figure 3 is that the trend of the three-dimensional obstacles is different from that of two-dimensional obstacles. The transition for the latter flows is sharp, indicating a different kind of instability. The inflectional point of the  $u_1$  profile, in the separation bubble, causes the growth of the disturbances in the whole span. For the three-dimensional obstacles the disturbances are the vortical structures generated by the side walls of the obstacles, producing other patches of vorticity which spread laterally to fill-up the entire region. Later on flow visualizations are used to describe the different physics.

For the three-dimensional obstacles  $R_k = U_k k / \nu$  ( $U_k$  is the value of  $u_1$  at

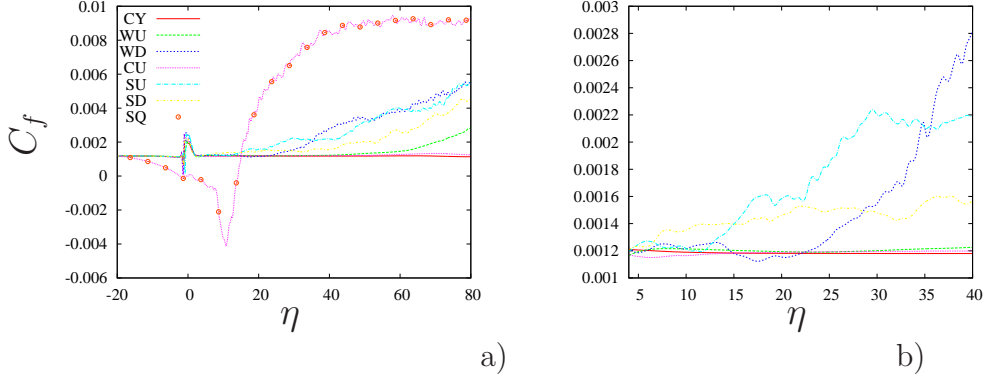


Figure 3: Streamwise profiles of  $C_f$  at  $Re = 5500$ ; a) in the whole length, b) in a region behind the obstacle to see the location of the transition.

the center of the obstacle and at  $x_2 = k$ ) has been evaluated. Flow visualizations show small differences of  $u_1$  among the different type of obstacles, with  $R_k$  varying between 474 and 512, the same range found by Klebanoff *et al.* [17] in several experiments. Since for some obstacle the transition occurs and for others does not, it follows that  $R_k$  is not the appropriate quantity to establish the transition. A better quantity then should be found. Orlandi [20] in two-dimensional channel demonstrated that  $u'_2$  at the edge of the obstacle produces a  $\tilde{u}'_2|_k$  varying in time. After a transient  $\tilde{u}'_2|_k$  was reaching a steady or unsteady condition depending on the  $Re$  number. In the latter case, characteristic of a fully turbulent flow, the averaged  $\tilde{u}'_2|_k^+$  in the two homogeneous directions was greater than a threshold value equal to 0.2. For boundary layers  $\tilde{u}'_2|_k$  is evaluated by averaging in time and in  $x_3$ . It varies in  $x_1$  then it may indicate whether and where the transition occurs. Figure 4a shows that in the laminar region, before the obstacle, with the small disturbances added  $\tilde{u}'_2|_k$  is practically negligible. At the obstacle a large jump, related to the thin shear layer forming on the top of the obstacle appears. For



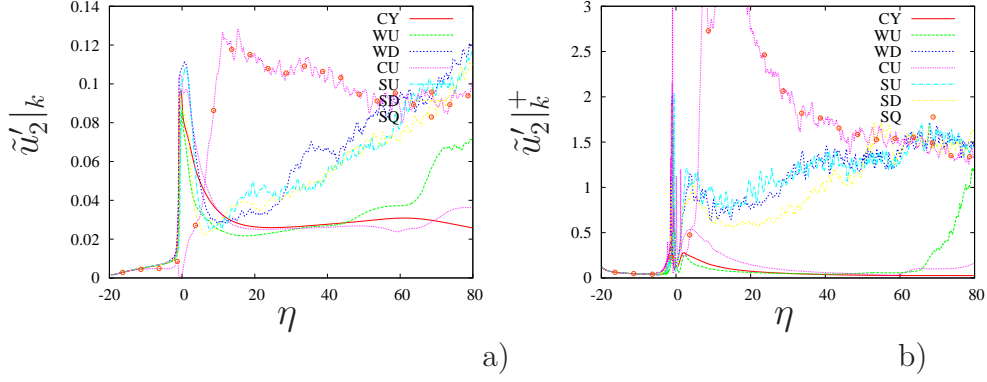


Figure 4: Streamwise profiles of a)  $\tilde{u}'_2|_k$  at  $Re = 5500$ ; b)  $\tilde{u}'_2|_k^+$

viscous effects  $\tilde{u}'_2|_k$  decreases downstream and for certain obstacles it grows again to lead to the turbulent regime. For the *WU* obstacle this happens at  $\eta \approx 60$ , and, for *CU*, it may occur at  $\eta > 80$ . Figure 4a, however, stresses the improbability to have a turbulent regime for *CY*. For the other three-dimensional obstacles a growth similar to that for *WU* is predicted, which at  $\eta \approx 60$  leads to a  $\tilde{u}'_2|_k$  greater than that for the two-dimensional obstacle.

Numerical and experimental investigations, by different research groups, are currently devoted to understand, in channels, pipes and boundary-layers, the reasons of the different trends of the maxima of the normal stresses with the increase of  $Re$ . The common view is that for channels and pipes the dependence is weak and the value is close to 1, for boundary layers the dependence is stronger and the values are slightly higher ( $\approx 1.2$ ) see Jimenez, & Hoyas [14]. Figure 4b shows that, at this low  $Re$ , despite the different trend, for the three- and the two-dimensional obstacles  $\tilde{u}'_2|_k^+$  tend towards the value typical of boundary layers. For the other geometries, generating small disturbances,  $\tilde{u}'_2|_k^+$  decreases for  $\eta > 5$ , then if it increases again and it reaches

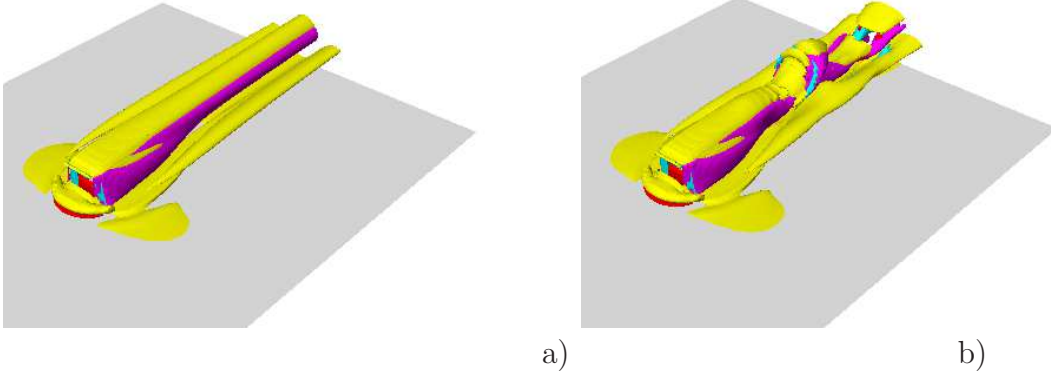


Figure 5: Surface contours of  $\omega_3 = -2.5$  yellow and  $\omega_3 = 2.5$  red superimposed to  $\omega_2 = -2$  cyan and  $\omega_2 = 2$  magenta a) cube  $Re = 5500$ , b)  $SU$  at  $Re = 5500$ .

$\tilde{u}'_2|_k^+ \approx 0.2$  it can be asserted that transition to turbulence occurs. The value 0.2 is close to the threshold value found by Orlandi [20] in transitional channels. It is important to clarify that for boundary layers over smooth walls encountering a single obstacle  $\tilde{u}'_2|_k^+$  varies in  $x_1$  therefore it can not be considered a threshold parameter to detect the transition. The result here found could help in the design of the shape of the obstacle, which should produce the highest value for  $\tilde{u}'_2|_k$ .

Flow visualizations of the vorticity field surrounding the obstacle may explain the different behaviors discussed for the three-dimensional obstacles. The  $CU$  and the  $SU$  cases are analysed, the first does not lead to transition near the obstacle, the latter does. The visualization in figure 5a and figure 5b emphasizes the important role of  $\omega_2$ , related to the spanwise gradients of  $u_1$  in presence of three-dimensional obstacles. Figure 5a does not produce a sinuous instability on  $\omega_2$ , the thin  $\omega_2$  layers roll-up remaining stable for a long distance. The head of the horses shoe vortex (red structure) at the

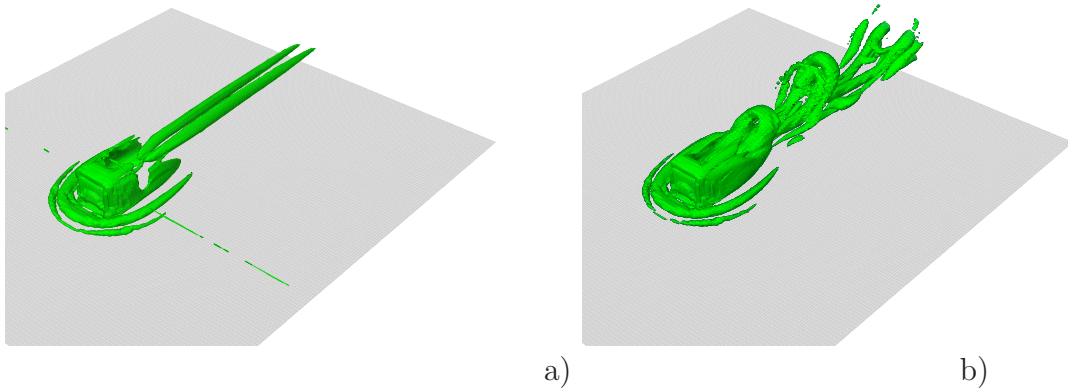


Figure 6: Surface contours of surface contour of  $\lambda_2 = 1$  a) cube  $Re = 5500$ , a)  $SU$  at  $Re = 5500$ .

bottom of the front face does not play a role. This figure leads to conclude that in order to promote the transition the shape of the obstacle should create vortical structures with a strong tendency to become unstable. Figure 2 showed that for the half cylinders ( $SU$ ) the thin regions with a clustering of  $u_1$  isocontours are curved and consequently unstable. The comparison between figure 5b and figure 5a shows equal vorticity layers in front of the obstacle. The circular shape of the side wall promotes the instability and the breakdown of the  $\omega_2$  and  $\omega_3$  layers. Flow structures are, usually, visualised by the  $\lambda_2$  surface contours (the imaginary part of the complex conjugate eigenvalue of the velocity gradient tensor), in figure 6a and figure 6b this quantity highlights the horseshoe vortex and a series of hairpins downstream the obstacle for the  $SU$ , while for the  $CU$  there is a similar horseshoe vortex and two circular vortices behind the obstacle. These structures have been visualised and studied by Acarlar & Smith [1]. More recently a forest of hairpins were visualised in the DNS of transitional boundary layers (Wu & Moin [33]). The  $\lambda_2$  detects the tubular structures which are the structures

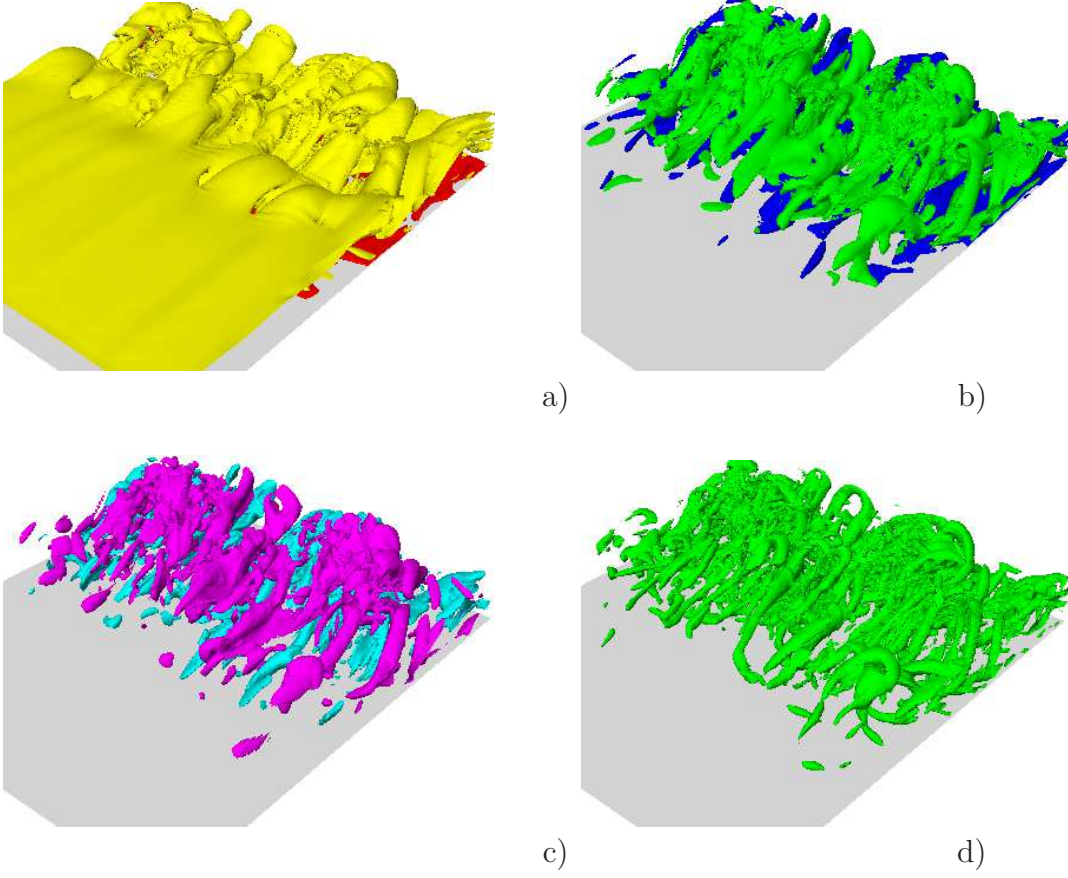


Figure 7: Surface contours for the case  $SQ$  at  $Re = 5500$ : a)  $\omega_3 = -2.5$  yellow and  $\omega_3 = 2.5$ , b)  $\omega_1 = -2$  blue and  $\omega_1 = 2$  green c)  $\omega_2 = -2$  cyan and  $\omega_2 = 2$  magenta d)  $\lambda_2 = 2$ .

less important to drive the instability and the energy cascade characteristic of turbulent flows. Figure 5 together with figure 6 indicate that the rollup of the  $\omega_2$  layers contributes to the legs, the rollup of the  $\omega_3$  sheets to the head of the hairpins.

These visualizations are useful to highlight the differences among the three- and the two-dimensional obstacles. A square bar creates a thin vorticity layer at its top and a recirculating bubble below it. Figure 7a shows the formation of the thin  $\omega_3$  layer bending and breaking at a certain  $x_1$ . For the effect of the other two vorticity components the  $\omega_3$  layers form structures of circular shape. For two-dimensional obstacles  $\omega_1$  and  $\omega_2$  are similar (figure 7b and figure 7c). These components are generated as fast growing instabilities due to the inflectional point in the profiles of  $u_1(x_2)$ . The forest of hairpins depicted in figure 7d is similar to that in Wu & Moin [33]. From these visualizations the reasons of the sharp growth of the  $C_f$  in figure 4 are understood. The forest of hairpins is observed also by three-dimensional obstacles, but at large distances from the solid element. To investigate the analogies and the differences between two- and three-dimensional obstacles simulations at a higher  $Re$  are presented.

### 3.2. High Reynolds number

Having demonstrated that the shape of the obstacle affects the transition, it is worth to investigate whether the simulations with the tripping devices can produce turbulent boundary layers at a reasonable high Reynolds number. In the last decade the possibility to use clusters with a large number of processors allowed to get DNS competing with laboratory experiments. Hoyas & Jimenez [12], for plane channels, had results up to  $R_\tau = 2000$ . This

$Re$  is smaller than those in laboratory experiments, nevertheless for the difficulty to have accurate measurements at  $R_\tau = 2000$  the results were useful to the fluid dynamics community. In particular for the scholars interested to the  $\tilde{u}'_2$ , to the vorticity rms, and to high order statistics. Regarding boundary layers, the largest  $R_\tau$  was simulated by Schlatter *et al.* [27] at  $R_\theta = 4300$  ( $R_\theta$  is the Reynolds number based on the momentum thickness) and results at higher  $R_\theta$ , in progress, were presented at conferences. For boundary layers it is easier to reach high  $R_\theta$  in laboratories, as reported in the review by Smits *et al.* [29]. However, the numerical simulations helped to understand the reasons of certain erroneous conclusions due to the limitations of the size of the probes. The present simulations reached  $R_\theta \approx 1500$ , and, to our knowledge are the first one to reproduce the turbulent boundary layers generated by tripping devices.

Simulations for a square bar and for a cube were performed at  $Re = 7500$  in a domain with  $L_1 = 51.2$  and  $N_1 = 1024$ ;  $L_3$  was the same as in the previous section but the number of points in  $x_3$  were doubled. In the normal direction the resolution was the same, in fact with 160 points, close to the outlet section, the first grid point is at  $y^+ = 0.845$ . The comparison between the square bar and the cube showed that, even for the square bar, only for certain statistics, a fully turbulent condition was achieved. For the square bar a further simulation more resolved in  $x_1$  and in a longer domain ( $L_1 = 68.2$ ) ( $N_1 = 2048$ ) was performed. In the normal directions the better resolution was obtained with  $L_2 = 9$  and 192 points. In wall units the resolution in the streamwise and spanwise directions, in the fully turbulent region, is respectively equal to 10.5 and 2.7.

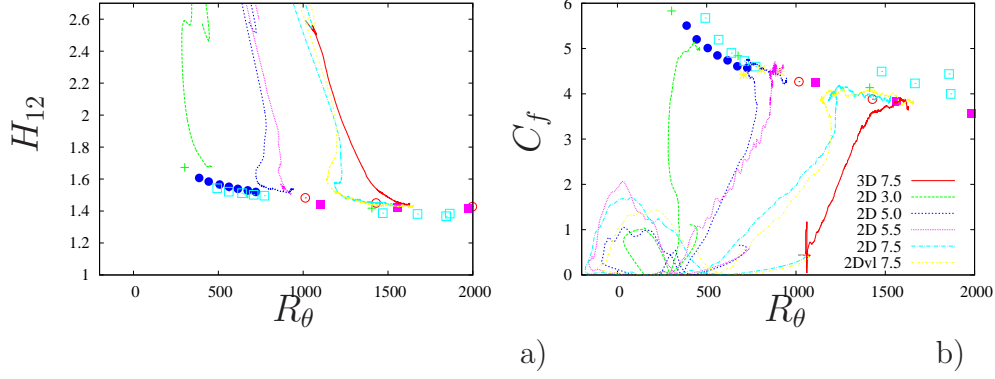


Figure 8: a) Shape factor  $H_{12}$ , b) friction factor  $C_f$  as function of  $R_\theta$ , the symbols are the data in Schlatter & Orlu [28] and the lines the present simulations as indicated in the insert.

Schlatter & Orlu [28] compared the variations of the shape factor  $H_{12}$  and  $C_f$  with  $R_\theta$  with those by other simulations, showing discrepancies but generally the same trend. They reported the values of the fully turbulent regime. The present simulations, including the transition, highlight the trend towards the fully turbulent regime. Figure 8a reproduces the decrease of  $H_{12}$  from the laminar to the turbulent value, which reaches the values of Schlatter & Orlu [28] at different  $R_\theta$ . For the three-dimensional obstacles the values with the cube at  $Re = 7500$  show that the trend for the cube differs from that, at the same  $Re$ , of the square bar. For the latter geometry small differences in the transitional regime are observed, but all the simulations in the fully turbulent regime give  $H_{12}$  in good agreement with that of Schlatter & Orlu [28]. Figure 8b shows a similar agreement for the  $C_f$ . Here the negative values for  $R_\theta$  account for the separation bubble. For the square bars at  $Re = 7500$  small differences in the  $C_f$  are encountered in the transitional regime, but independently from the resolution ( $vf$  in the insight of figure 8b

indicates the more resolved) in the fully turbulent regime the agreement with Schlatter & Orlu [28] data extends for a wide range of  $R_\theta$  values.

As previously mentioned, the reason of the different trends to the turbulent regime for two- and three-dimensional obstacles is linked to the different type of instability. This is qualitatively described by the velocity contours at different distances from the obstacle. Figure 9a shows that the no-slip condition on the side of the cube produces two low-speed streaks, better depicted by the  $\omega_2$  contours in a horizontal plane at a distance  $x_2 = 0.05$ , in wall units approximately equal to 17 (figure 9e). Further downstream other vortex couples form, which imply an array of low and high speed streaks. In the first two  $x_2 - x_3$  planes, in figure 9a, the undulation at the edge of the boundary layer is almost negligible, indicating small fluctuations of  $u_2$ , quantified by  $u_2$  contours in figure 9c. These disturbances at the fourth and fifth sections are enough strong to deform the  $u_1$  contours at the edge of the boundary layer in figure 9a. The  $\omega_2$  contours in figure 9e show the end of the spreading at the fifth section and the moderate  $u_2$  ejections, until there, are depicted in figure 9c. This figure, further downstream, shows coherent ejections going from the near wall region up to the edge of the boundary layer. These are the large structures that recently attracted the interest of a large number of researchers cited by Pirozzoli *et al.* [26]. A more quantitative analysis of the effects of the large scale structures has been described by Pirozzoli *et al.* [26] for Couette flows where the turbulent kinetic energy production, in the central region, facilitates the formation of the large structures similar to those in the boundary layers.

The transitional region is different for the square bar, the black region in



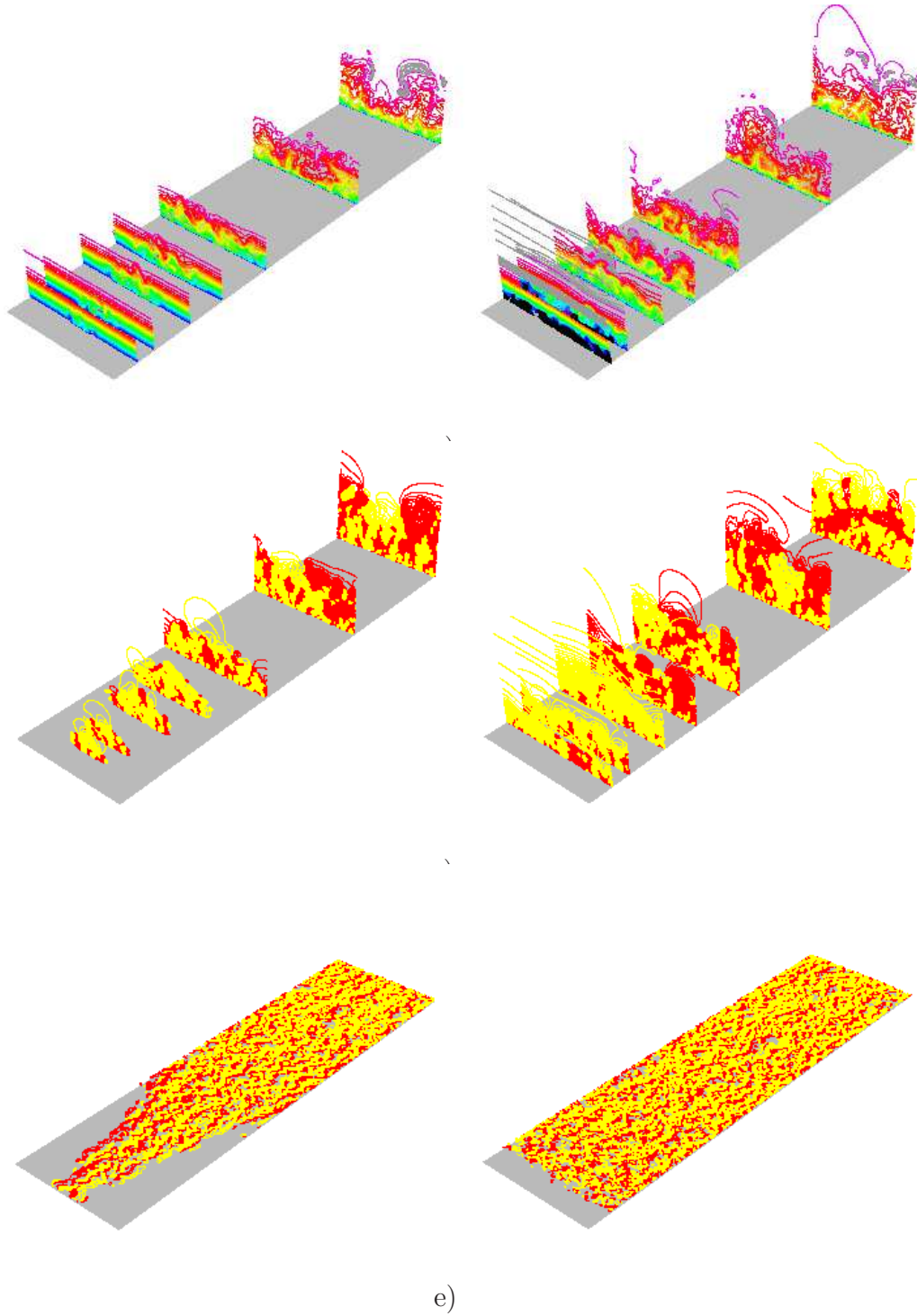


Figure 9: Contours of a), b)  $u_1$  and c), d)  $u_2$  at different  $x_2 - x_3$  planes for the cube in the top figures and for square bars in the bottom at  $Re = 7500$ ;  $\Delta u_1 = 0.05$  for positive values  $\leq 1$  colour from blue to red,  $\Delta u_1 = 0.005$  for values  $\geq 1$  grey and black for negative values;  $\Delta u_2 = 0.005$  yellow negative red positive, in e) and f) contours of  $\omega_2$  at  $x_2 = 0.05$  in a  $x_1 - x_3$  plane yellow negative and red positive with  $\Delta \omega_2 = 1$ .

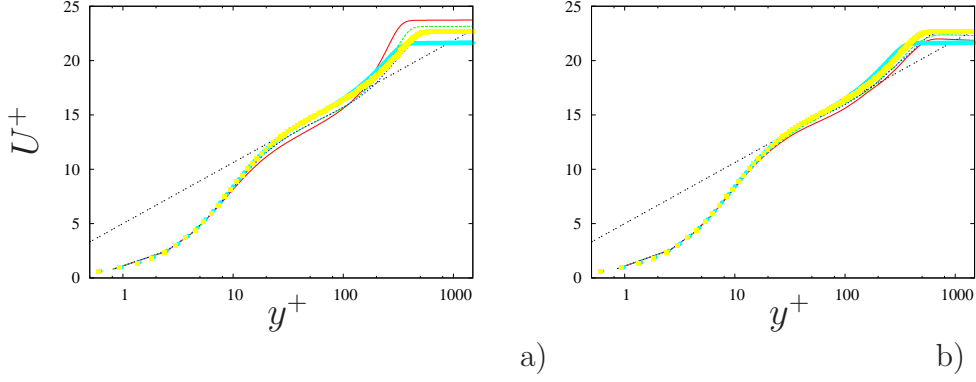


Figure 10: Mean streamwise velocity profile in wall units: a) for the cube ( $CU$ ), b) for the square bar ( $SQ$ ) at three stations (lines) and compared with the (solid symbols) Schlatter *et al.* [27] data at  $R_\tau = 1000$  and  $R_\tau = 1400$ .

the contour plots in figure 9b highlights the large separation bubble which does not reattach uniformly in agreement with the contours in the second  $x_3 - x_2$  plane. The comparison between the contours at the fourth plane in figure 9c and figure 9d stresses large undulations in the outer layer for the two-dimensional obstacle, due to the fast growing disturbances promoted by the inflectional point in the profiles of  $u_1$ , located in the black region in figure 9b. The contours of  $u_2$  in the fourth  $x_2 - x_3$  plane in figure 9d confirm the strong interaction between the near wall and the outer regions. This observation is corroborated by the wider region where the profiles of  $\tilde{u}'_2$ , for wall bounded flows are constant with respect to that for  $\tilde{u}'_1$  and  $\tilde{u}'_3$ . The contours of  $\omega_2$  in figure 9f show that the near wall streaks close to reattachment line are short, and long in the fully turbulent region.

To have a quantitative measure of the distance necessary to get the fully turbulent regime the profiles in wall units may help. In boundary layers the correct averaging is in time and in the spanwise direction. A further averaging

in  $x_1$  for a dimensionless length equal to 0.1, accounting for approximately 50 profiles, allows to store less fields. The profiles are calculated at three distances from the obstacle: equal to  $115k$ ,  $140k$  and  $165k$ . In this range  $1200 > R_\theta > 1400$  therefore the data of Schlatter *et al.* [27] at  $R_\theta = 1000$  and  $R_\theta = 1400$  are considered. Figure 10a shows that for the cube at the first station (red line) the profile of  $U^+$  does not have a satisfactory log law, further downstream the agreement is better, but the profiles fit the log law with  $B = 4.8$  instead of  $B = 5.0$ . For the square bar a much better agreement is observed in Figure 10b where only at  $x_1 = 115k$  the correct log law is not fitted. The mean velocity profiles approach faster the fully turbulent one, however a fully turbulent regime is established when all the statistics have the appropriate profile.

In figure 11 the profiles of the normal stresses at the same locations of the  $U^+$  in figure 11 reinforce the observation that the fully turbulent condition is reached at a shorter distance for the two- than for the three-dimensional obstacles. The profiles in the near wall region converge faster implying that the near wall structures form closer to the disturbance, and that the large structures in the log and in the outer regions are affected by the inlet conditions. The comparison among the three stresses highlights large deviations of  $\tilde{u}'_2$  from the correct value, and this fact corroborates our view that, in wall bounded flows, this stress accounts for the changes at the wall, as it was shown by Orlandi *et al.* [23] and for the disturbances affecting the outer region.

Figure 12 shows large differences between the Schlatter *et al.* [27] results and the present ones. The reason is related to the insufficient  $L_1$  to get

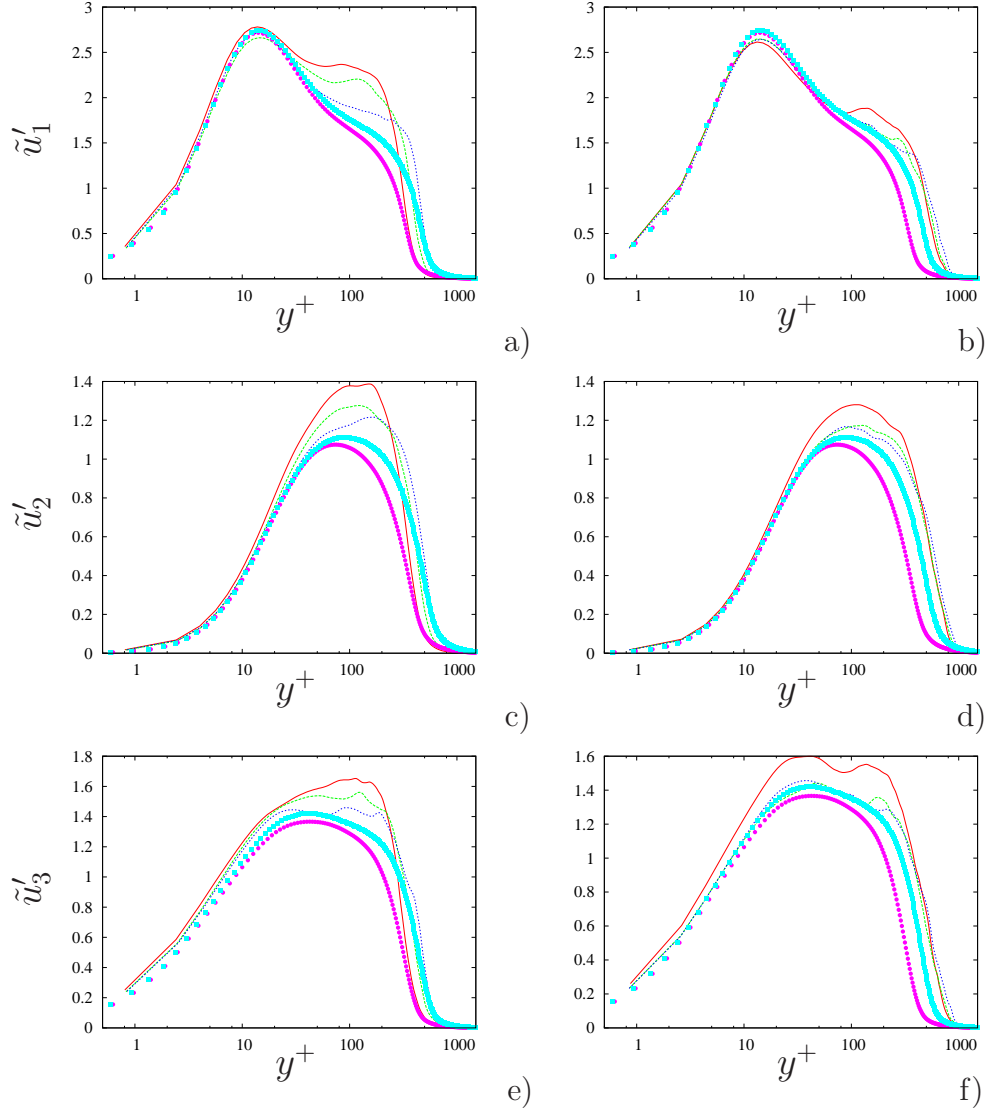


Figure 11: Normal stress velocity profiles in wall units: a), c), e) for the cube (*CU*), b), d), f) for the square bar (*SQ*) at three stations (lines) and compared with the (solid symbols) Schlatter *et al.* [27] data at  $R_\tau = 1000$  and  $R_\tau = 1400$ .

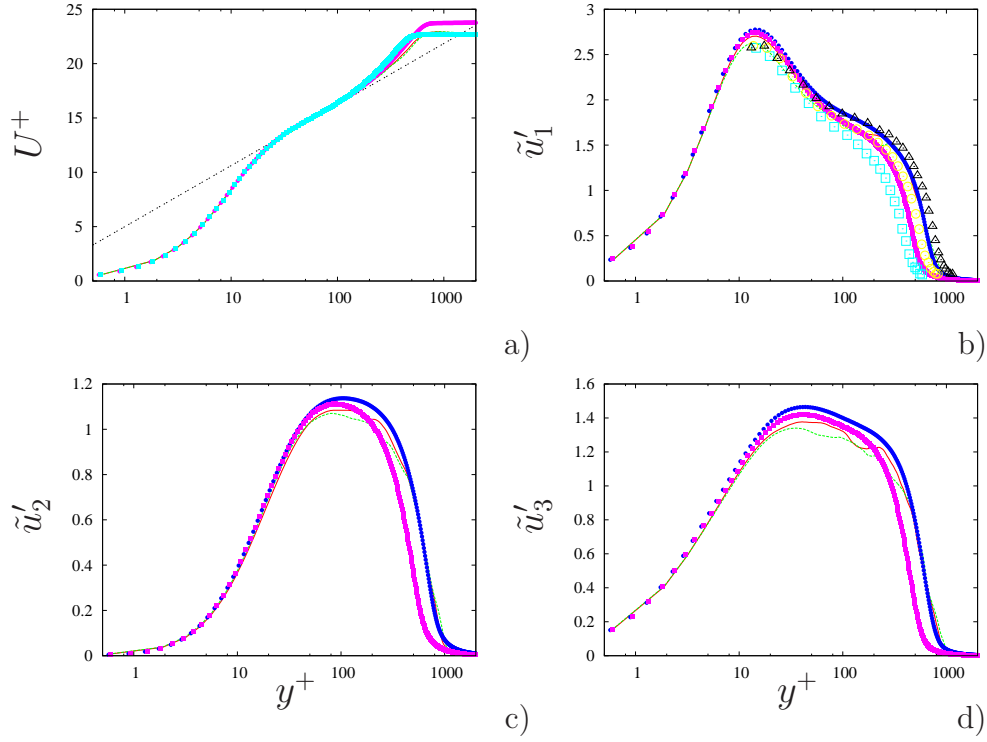


Figure 12: a) Mean streamwise velocity and b), c), d) normal stress velocity profiles in wall units for the square bar ( $SQ$ ) at two stations (lines) ( $R_\tau \approx 1600$ ) compared with the (solid symbols) Schlatter *et al.* [27] data at  $R_\tau = 1000$  and  $R_\tau = 2000$ . and the Erm & Joubert [7] (open symbols) experiments at  $R_\tau = 1000, 1500$  and  $R_\tau = 2000$ .

the fully turbulent regime, to the smaller resolution than that in Schlatter *et al.* [27] and to the different type of disturbances. Therefore, a more refined simulation, with the parameters previously reported, was performed for the square bar, having observed to be the most efficient to promote the transition. This simulation is a first attempt to reproduce the most complete and documented experiments in turbulent boundary layers by Erm & Joubert [7]. The reproduction of the small obstacles used in the experiments requires an enormous amount of computational time, therefore in the discussion it should be recalled that the height of the tripping device ( $k/\delta = 0.25$ ) is greater than that in the experiment ( $k/\delta = 0.1$ ). This difference together with the limitations in  $L_1$  affect the wake region. Far from the obstacles  $R_\theta \approx 1600$  is a value intermediate between the  $R_\theta = 1000$  and  $R_\theta = 2000$  by Schlatter *et al.* [27]. The very good agreement for  $U^+$  is appreciated in figure 12a. Near the wall the stresses (figure 12b,d) are slightly smaller than those by Schlatter *et al.* [27]; the reason may be related to the different resolution. The small oscillations in the outer regions, in large part, are due to the large scales produced by the obstacle. In a longer domain these oscillations disappear, but to show it a very large CPU is required. These oscillations, due to the trip, are not encountered in simulations based on a recycling procedure, where these long-lived structures, in the outer region, are not continuously introduced. At  $R_\theta \approx 700$ , Erm & Joubert [8] claimed that differences with the Spalart [31] DNS were related to the tripping. In the experiments the height was  $0.1\delta$ , therefore, with an obstacle of height  $0.25\delta$  it is reasonable to find in the outer layer differences between the present and the results obtained with the recycling procedure.

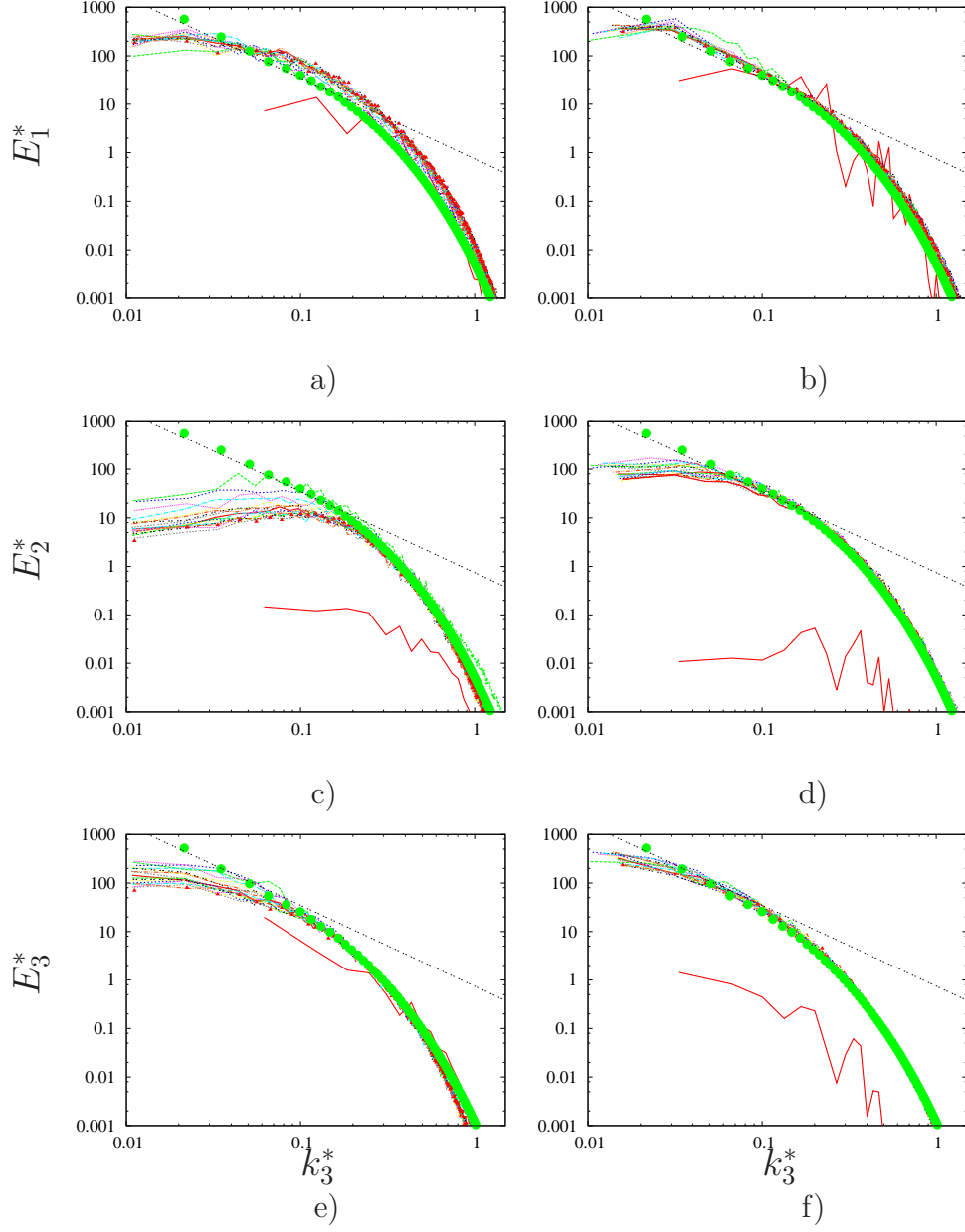


Figure 13: Spectra in kolmogorov units a), c), e) at  $y^+ = 25$ , b), d), f) at  $y^+ = 110$  in the spanwise direction (lines), compared with isotropic turbulence at  $R_\lambda = 100$  (Jimenez *et al.* [13]) open symbols, a), b), c), d) transverse e), f) longitudinal.

To demonstrate that the turbulent fields are fully resolved it is worth looking at the spectra in Kolmogorov units, if a collapse in the exponential range with those of isotropic turbulence occurs it means that a true DNS is performed. The agreement in the whole range implies the reproduction of the turbulent energy cascade process. The velocity spectra in the span-wise direction are compared with the longitudinal and transverse spectra by Jimenez *et al.* [13] at  $R_\lambda = 98.7$ . The spectra at  $y^+ = 25$  at different locations, separated by a distance equal to  $3.2\delta$  starting from  $x_1 = 6.4$ , are presented in figure 13. At the first location, inside the separation bubble, the spectra are completely different than the others. In the transitional and in the fully turbulent regions a good collapse of the spectra at high  $k_3$  is obtained, corroborating the previous statement that the small scale adjust in a short distance. In agreement with figure 13 the energy containing scales for  $u_1$  are those adjusting faster. Instead those for  $u_2$  require a longer distance to reach the streamwise independence in the fully turbulent regime (indicated by small triangles in figure 13). The spectra for  $u_1$  in the log region at  $y^+ = 110$  (the figures on the right of figure 13) have a reasonable wide inertial range. In addition, a better collapse of the spectra of  $u_2$  is achieved (figure 13d), and the tendency towards isotropic turbulence is emphasised in figure 13d and figure 13e. From the computational side the last two figures are a convincing proof that these simulations are true DNS, having resolved scales of size close to the Kolmogorov scales.



## 4. Conclusions

One common way to promote the transition of laminar boundary layers is through tripping devices inserted at a certain distance from the leading edge. A large number of experiments were devoted to find a critical Reynolds number, but a systematic study of the influence of the shape of the obstacle was never attempted, even if it was requested by Klebanoff *et al.* [17]. This lack of data motivated the present study and from the results achieved it was clear that a critical Reynolds number based on the velocity at the top of the obstacle ( $U_k$ ) and on its height  $k$  could not be the satisfactory quantity marking the transition. In fact it is reasonable to expect that by varying the shape of the obstacle,  $U_k$  could not drastically change. This has been confirmed by the present simulations, but in the mean time it was observed that for certain shapes there was transition and for others not. In agreement with the previous results in rough channels (Orlandi [20]) it has been observed that the transition occurs when  $\tilde{u}'_2|_k^+$  is greater than a threshold value. In the channel the periodic conditions lead to an easy determination of the threshold value. In boundary layer the determination is more critical for the streamwise evolution of  $\tilde{u}'_2|_k$ . However the numerical simulations demonstrate that, in analogy to the case of a normal wall jet where the transition is linked to the exit velocity, also for solid obstacles if the amplitude of  $\tilde{u}'_2|_k$  is greater than a threshold limit the transition occurs.

The DNS furnishes the vorticity field, and flow visualizations of the three vorticity components lead to conclude that  $\omega_2$  is the most important, modifying the  $\omega_3$  sheet generated at the top of the obstacle. The head of the horseshoe vortex generated by the obstacle does not contribute to the tran-

sition. It has been, also understood that for isolated elements the transition is enhanced by geometries which create curved vorticity sheets. To reach a fully turbulent conditions the wake generated by isolated obstacles expand laterally by the generation of opposite sign vorticity at the wall. The entire process can be summarised as the wake instability mentioned by Klebanoff *et al.* [17], which differs from the inflectional instability occurring in presence of two-dimensional obstacles. The present DNS demonstrated that the latter instability is more efficient to produce a fully turbulent regime, and therefore simulations with square bars have been performed at high  $Re$  and the results have been compared with previous numerical simulations, and laboratory experiments.

The most refined simulation, with a two-dimensional trip, produced mean velocity and turbulent stresses profiles in a good agreement with those achieved in DNS with recycling procedures or with ad hoc inlet disturbances. The results suggest that the numerical method here used is an efficient tool to create a data base with all the ingredients necessary to understand the differences among wall bounded flows in pipe, channels and boundary layers. In the simulations "hot wires" measuring the three velocity, and vorticity components, together with the pressure have been inserted. The temporal data can be used to understand the differences on the spectra obtained by the Taylor hypothesis and those evaluated in the spanwise directions. The latter spectra were presented as a proof of the reproduction of the physics of turbulent flows characterised by an universal exponential range. The temporal signals may help to understand the quality of a hot wire, having observed that the smallest Kolmogorov scales have been captured in the numerical simulations.

The present numerics is not appropriate to reproduce tripping devices of smaller height, requiring large computational resources. To achieve this goal, with limited resources, modifications of the numerics with non-uniform grids in all three directions are necessary. In this way the increased resolution near the obstacle allows to create the vorticity sheets driving the transition. For incompressible flows this is a difficult task, but it is feasible with non-uniform grids in  $x_1$  and  $x_2$ . Our aim is to introduce these modifications in order to reproduce the experiments by Erm & Joubert [7] with a two-dimensional trip device with  $k/\delta = 0.1$ . For three-dimensional obstacles a good clustering can be obtained by using the compressible code at low Mach number used by Bernardini *et al.* [3]. In these circumstances the small time steps require a much large computational time than that used for the simulations here discussed.

## 5. Acknowledgments

The support of a MIUR 60 % grant is acknowledged. The computer time was given by CASPUR and by CINECA.

## References

- [1] Acarlar, M. & Smith, C. 1987 A study of hairpin vortices in a laminary boundary layer. Part 1. Hairpin vortices generated by a hemisphere protuberance. J. Fluid Mech. 175, pp 1–41.
- [2] Bake, S., Meyer, D. G. W. & Rist U. 2002 Turbulence mechanism in Klebanoransition: a quantitative comparison of experiment and direct numerical simulation J. Fluid Mech., 459, pp. 217-243.

- [3] Bernardini, M., Pirozzoli, S. & Orlandi, P. 2011 Compressibility effects on roughness-induced boundary layer transition Proceedings TSF7 , in press on Intl J. Heat Fluid Flow
- [4] Burattini P., Leonardi S., Orlandi P. & Antonia R.A. 2008. Comparison between experiments and direct numerical simulations in a channel ow with roughness on one wall. *J. Fluid Mech.* Vol. 600, pp. 403-426.
- [5] Dryden, H. 1953 Review of published data on the effect of roughness on transition from laminar to turbulent flow, *J. Aeronaut. Sci.*, 20, pp. 477-482
- [6] Emmons,. w. 1951 The laminar-turbulent transition in a boundary layer. Part I, *J . Aero. Sci .* 18, pp. 490.
- [7] Erm, L.P. & Joubert, P.N., 1991 Low-Reynolds number turbulent boundary layers *J. Fluid Mech.*, vol. 230, pp. 1-44.
- [8] Erm, L.P. & Joubert, P.N., 1992 Turbulent boundary layers at low-Reynolds number 11th Australasian Fluid Mechanics Conferene. 7A-7.
- [9] Ergin, F. G. & White, E. B. 2006 Unsteady and transitional flows behind roughness elements, *AIAA J.*, 2006, 44, pp. 2504-2514
- [10] Fadlun, E. A., Verzicco, R., Orlandi, P.& Mohd-Yusof, J., 2000 Combined immersed boundary finite-difference methods for three-dimensional complex flow simulations, *J. Comput. Phys.*, **161**, pp. 35–60
- [11] Furuya, Y., Miyata, M. & Fujita, H. 1976. Turbulent boundary layer

- and flow resistance on plates roughened by wires. *J. Fluids Eng.* **98**, pp. 635–644.
- [12] Hoyas, S. & Jimnez, J. 2006 “Scaling of the velocity fluctuations in turbulent channels up to  $Re_\tau = 2003$ ” *Phys. Fluids*. Vol. 18, 011702 (2006).
  - [13] Jimenez, J., Wray, A.A., Saffman, P.G. & Rogallo, R.S., 1993 The structure of intense vorticity in isotropic turbulence. *J. Fluid Mech.*, vol. 255, pp. 65-90.
  - [14] Jimenez, J., & Hoyas, S., 2008 Turbulent fluctuations above the buffer layer of wall-bounded flows *J. Fluid Mech.*, vol. 611, pp. 215-236
  - [15] Kendall, J., 1981 Laminar boundary layer velocity distortion by surface roughness: Effect upon stability. AIAA Paper 81-0195.
  - [16] Klebanoff, P., Tidstrom, K. D. & Sargent, L. M. 1962 The three-dimensional nature of boundarylayer transition. *J. Fluid Mech.* 12, pp. 1-34.
  - [17] Klebanoff, P., Cleveland, W.G., & Tidstrom, K. D. 1992 On the evolution of a turbulent boundary layer induced by a three-dimensional roughness element *J. Fluid Mech.* (1992), vol. 237, pp. 101-187
  - [18] Lee, J. H., Sung, H.K. & Krogstad, P. A. 2011 Direct numerical simulation of the turbulent boundary layer over a cube-roughened wall *Journal of Fluid Mechanics*, 2011
  - [19] Orlandi, P. 2000. *Fluid Flow Phenomena : A Numerical Toolkit*, Kluwer.

- [20] Orlandi P. 2011 DNS of transitional rough channels Journal of Turbulence. Vol. 12 pp. 1-20
- [21] Orlandi P. & Leonardi S. 2006. DNS of turbulent channel flows with two- and three-dimensional roughness. Journal of Turbulence. Vol. 7, No. 53, 1468-5248.
- [22] Orlandi P., Leonardi S., & Antonia A.R. 2006. Turbulent channel flow with either transverse or longitudinal roughness elements on one wall. *J. Fluid Mech.* **561**, pp. 279-305.
- [23] Orlandi P., Leonardi S., Tuzi R. & Antonia R.A., 2003, DNS of turbulent channel flow with wall velocity disturbances Phys. Fluids. Vol. 15, pp. 3497–3600.
- [24] Pauley, L.L., Moin, P. & Reynolds, W.C. 1992 The structure of two-dimensional separation *J. Fluid Mech*, **220**, pp. 397–441.
- [25] Pirozzoli, S., Bernardini, M. & Grasso, F., 2010 On the dynamical relevance of coherent vortical structures in turbulent boundary layers, *J. Fluid Mech*, 648 , pp. 325 - 349
- [26] Pirozzoli, S., Bernardini, M. & Orlandi, P. Large-scale motions and inner/outer layer interactions in turbulent Couette-Poiseuille flows, *J. Fluid Mech* 680 , 2011, pp. 534 - 563
- [27] Schlatter, P., Li, Q., Brethouwer, G., Johansson, A. V. & Henningson, D. S. 2010 Simulations of spatially evolving turbulent boundary layers up to  $Re = 4300$ . Intl J. Heat Fluid Flow 31, pp. 251-261

- [28] Schlatter, P., & Orlu, R.S., 2010 Assessment of direct numerical simulation data of turbulent boundary layers J. Fluid Mech. (2010), vol. 659, pp. 116-126.
- [29] Smits, A.J., McKeon, B.J. & Marusic, I. 2011 High Reynolds Number Wall Turbulence Annual Review of fluid mechanics. 43: pp. 353-375
- [30] Simens, M. P., Jimenez, J., Hoyas, S. & Mizuno, Y. 2009 A high-resolution code for turbulent boundary layers. J. Comput. Phys. 228, pp. 4218-4231
- [31] Spalart, P.R. (1988) Direct simulation of a boundary layer J. Fluid Mech. **187**, pp. 61-98
- [32] Tani, I., Komoda, A. , Komatsu, Y. & Iuchi, M. 1962 Boundary layer transition by isolated roughness. Aero. Res. Znst. Rep. 375. Tokyo University.
- [33] Wu, X. & Moin, P. 2009 Direct numerical simulation of turbulence in a nominally zero-pressure-gradient flat-plate boundary layer Journal of Fluid Mechanics, 2009